| 2           | Oxidative state of MoO <sub>3</sub> nanoparticles affect dissolution and visible-light photocatalytic activity   |
|-------------|--|
| 3<br>4<br>5 | Janire Peña-Bahamonde <sup>1</sup> , Chunzheng Wu <sup>2</sup> , Sofia Fanourakis <sup>1,3</sup> , Stacey Louie <sup>1</sup> , Jiming Bao <sup>2</sup> and Debora F. Rodrigues <sup>1,3*</sup> |
| 6           | <sup>1</sup> Department of Civil and Environmental Engineering, University of Houston, Houston, TX   |
| 7           | 77204 - 4003   |
| 8           | <sup>2</sup> Department of Electrical Engineering, University of Houston, Houston, TX 77204 – 4003   |
| 9           | <sup>3</sup> Department of Materials Science and Engineering, University of Houston, Houston, TX 77204   |
| 10          | -4003  |
| 11<br>12    | * Corresponding Author: Debora F. Rodrigues, email: dfrigirodrigues@uh.edu   |
| 13          |  |
| 14          |  |
| 15          |  |
| 16          |  |
| 17          |  |
| 18<br>19    |  |
| 20          |  |
| 21          |  |
| 22          |  |
| 23          |  |
| 24          |  |
| 25          |  |

28

29

30

31

32

33

34

35

36

37

38

39

40

41

42

43

44

45

46

47

48

#### Abstract

The role of shape, dissolution, and chemical properties of MoO<sub>3</sub> nanomaterials with visible light photocatalytic activity are still largely unknown. In the present study, we investigate three MoO<sub>3</sub> nanomaterials with different shapes and chemical properties, i.e. nanorods, nanowires, and nanosheets, as well as their dissolution products under different pH values, since pH directly affects dissolution. The results showed that different morphologies of MoO<sub>3</sub> presented different solubility behaviors at different pH values with the highest solubility at pH 10. The dissolution of these nanoparticles depends on the oxidative state and nature of the Mo-O bonds. The photocatalytic properties of the nanoparticles also showed a pH-dependent behavior influenced by the nanoparticle dissolution. The photocatalytic experiments for the removal of methylene blue (MB) showed that the nanorods presented the best photocatalytic-based degradation activity while the nanowires (the one that dissolved the most) were able to decolorize MB the fastest. The dissolution seemed to affect the rate of the reaction but not the amount that was degraded. The amount degraded seems to depend on the different oxidation states of the Mo, i.e. higher abundance of Mo<sup>6+</sup>. The evaluation of the MoO<sub>3</sub> photocatalytic degradation mechanisms was performed by the quantification of reactive oxygen species (ROS) produced by the nanoparticles as well as by measurements of the inhibition of photocatalytic degradation of MB in the presence of specific ROS scavengers. The results showed that the photogenerated holes in the nanomaterials is involved in the degradative process by allowing the production of hydrogen peroxide. Different techniques, such as UV-Vis Spectroscopy, ATR-FTIR, XPS, and HPLC allowed us to demonstrate that, not only the nanomaterial degrades MB, but also the dissolved ions from the

nanomaterial are involved in the degradation. In particular, the dissolved ions help during the degradation process by complexing with MB. This study demonstrates that the chemical and physical properties as well as the dissolution process of different MoO<sub>3</sub> nanoparticles can influence the photocatalytic properties of MoO<sub>3</sub> nanoparticles. Keywords: MoO<sub>3</sub>, nanorods, nanosheets, nanowires, pH dependency, dissolution, reactive oxygen species **Highlights:** 1. Synthesis and characterization of nanorods, nanowires, and nanosheets MoO<sub>3</sub> nanoparticles 2. Dissolution of MoO<sub>3</sub> nanoparticles at basic pHs. 3. Mo ion produces complexation and is also able to degrade MB. 4. The photogenerated holes in the nanomaterials play an important role in degradation of MB. 

### Introduction

70

71

72

73

74

75

76

77

78

79

80

81

82

83

84

85

86

87

88

89

90

91

92

Recently, MoO<sub>3</sub> nanoparticles have been described to present photocatalytic properties under visible light. The degradation of methylene blue [1][2] and orange II dye [3], methanol oxidation [4], epoxidation [5], gas sensing properties [6], supercapacitor [7], optical properties [8], and lithium storage capabilities [9] have been investigated with MoO<sub>3</sub> under visible light. The photocatalytic performance of MoO<sub>3</sub> has been associated to shape, size, and chemical properties. Different synthetic strategies have shown that MoO<sub>3</sub> exhibits h- and  $\alpha$ - phases. The h-phase corresponds to nanorods morphologies; while the α- phase corresponds to nanosheets and nanowires [10–12]. Control of the morphology and nanoparticle size can be achieved by varying different parameters, e.g. the concentration of reactants, time, temperature, pressure, and solvents. Despite the fact that visible light photocatalysis makes MoO<sub>3</sub> an attractive material for contaminant degradation, prior studies have demonstrated that reductive dissolution of MoO<sub>3</sub> can occur in aqueous systems [13,14], diminishing its utility for water treatment and other applications. However, a thorough study of the dissolution and photocatalytic activity of the various phases and morphologies of MoO<sub>3</sub> nanoparticle has not yet been conducted, to our knowledge. Many studies have shown that other types of nanoparticles, including silver [15,16], silica [17], ZnO [18,19], CeO<sub>2</sub> [19] nanoparticles (NPs), can dissolve. The stability of the nanoparticles in terms of dissolution will depend on several factors, such as presence of natural organic matter, ionic strength, and type of electrolyte, aggregation state, pH, and size [20]. In the case of organic matter, the dissolution can be increased or decreased by steric shielding or ligand-promoted processes, respectively. When ionic strength, type of electrolyte, or pH are altered the behavior of the particles can also change and lead to increased nanoparticle aggregation influencing the

exposed surface area to the media and dissolution. Size can also play a role, whereby smaller particles are more prone to dissolving than larger particles, as described by the well-known Ostwald-Freundlich equation. In the case of MoO<sub>3</sub>, it has been shown, that pH changes can play an important role in the dissolution of this nanoparticle [21]. Dissolution of the NPs can be expected to change the heterogeneous catalytic reactions that occur at the NP surface and perhaps even affect the production of reactive oxygen species (ROS). The dissolution behavior of the nanoparticles is critical in determining both the toxicity and reactivity of the nanoparticles. Previous investigations have shown that the production of reactive oxygen species (ROS) plays an important in photocatalytic reactions. The quantification of individual ROS is a prerequisite to elucidate actual ROS functions in photocatalysis. The production of different ROS by TiO<sub>2</sub> [22–25], graphene oxide [26], silver [27], ZnO [25,28], and iron oxide [29] is well studied. However,

25], graphene oxide [26], silver [27], ZnO [25,28], and iron oxide [29] is well studied. However, the production of ROS by photocatalysts induced by visible light, such as MoO<sub>3</sub>, have not been reported thus far. In the present study, we take into consideration the role of pH in the dissolution of MoO<sub>3</sub> nanoparticles as well as the effects of dissolution in ROS production and degradation of methylene blue (MB), as an example of a water contaminant, to understand the mechanisms of the photocatalytic degradation of MoO<sub>3</sub> nanoparticles. We hypothesize that MoO<sub>3</sub> nanoparticles with different material properties will show different propensities to dissolve, and that the dissolution behavior will then change the photocatalytic ability of the NPs.

### Materials and Methods

### 112 Materials

Ammonium molybdate tetrahydrate ((NH<sub>4</sub>)<sub>6</sub>Mo<sub>7</sub>O<sub>24</sub>·4H<sub>2</sub>O), nitric acid (HNO<sub>3</sub>), molybdenum powder (1-5 μm, ≥99.9%), hydrogen peroxide (H<sub>2</sub>O<sub>2</sub>), ethanol (EtOH), methanol (MeOH)

HPLC grade, furfuryl alcohol, terephthalic acid, Isopropanol (>99.7%), benzoquinone (AR grade), triethanolamine (>99.0%) and methylene blue were purchased from Sigma-Aldrich and were used as received. Glutathione and 5,5'-Dithiobis(2-nitrobenzoic acid) (Ellman's reagent) were supplied by Fisher Scientific.

### Synthesis

The MoO<sub>3</sub> nanomaterials were synthesized by the hydrothermal route using modified published procedures [3,30,31]. Briefly, the modifications were: the nanorod MoO<sub>3</sub> nanoparticles were prepared by dissolving 2.46 g of (NH<sub>4</sub>)<sub>6</sub>Mo<sub>7</sub>O<sub>24</sub>·4H<sub>2</sub>O in 20 mL of distilled water (DIW). To this solution, 5 mL of HNO<sub>3</sub> was added drop by drop. The solution was transferred to an 80 mL Teflon-lined stainless-steel autoclave and heated at 90°C. After 3 h of reaction a white precipitated was collected and washed several times with EtOH (70%) and then dried at room temperature.

Black MoO<sub>3-x</sub> nanosheets and nanowires were prepared according to the procedures reported by Yin et al. [31] with some modifications. For the nanosheets, 192 mg of molybdenum powder was added to a Teflon vessel (45 ml) containing 24 ml of ethanol under magnetic stirring. Then, 3 ml of H<sub>2</sub>O<sub>2</sub> was injected, and the mixture was stirred for 0.5 h to obtain a yellow solution. The Teflon vessel was then sealed in a stainless-steel autoclave, heated, and maintained at 160 °C for 14 h. The product was collected by centrifugation, washed with ethanol for several times, and finally dried under vacuum. The nanowires were prepared using the same procedure as the black nanosheets except using 384 mg of molybdenum powder, 30 ml of isopropanol, and 5 ml of H<sub>2</sub>O<sub>2</sub>.

### **Nanomaterial Characterization**

137

138 Crystallographic information of samples was determined by X-ray diffraction (XRD) (Philips 139 X'pert Pro X-ray diffractometer). The Cu K $\alpha$  radiation was used ( $\lambda = 1.54$  Å) at a scanning rate of 0.020° per second from 5° to 80° in 20. The voltage was set to 40 kV, and the current to 140 141 40 mA. Crystal sizes of the samples were estimated from the full-width at half-maxima 142 (FWHM's) of some intense XRD diffraction peaks using Scherrer's method. X-ray diffraction 143 (XRD) was measured using a Rigaku Smartlab with Cu K $\alpha$  radiation ( $\lambda = 1.5406$  Å). 144 Fourier-transform infrared spectroscopy (FTIR) was performed in a Thermo Scientific Nicolet 145 IS50 FTIR Spectrometer in the wavenumber range from 4000 to 500 cm<sup>-1</sup>. The ATR-FTIR was 146 employed to evaluate the interaction between MB-MoO<sub>3</sub> and MB-ion. After each reaction, 147 samples where centrifuged for collection of the pellet, which were subsequently freeze-dried. 148 The spectra were obtained on a Digilab FTS 7000 equipped with a HgCdTe detector from 4000 to 600 (cm<sup>-1</sup>) wavenumbers. 149 150 The morphology of crystal samples was examined by scanning electron microscopy (SEM). 151 Samples were coated with gold for 30 seconds (Denton Desk V) and then, observed by SEM 152 (Nova NanoSEM 230) at accelerating voltage equal to 5 kV at different magnifications. The size 153 of the nanomaterials was estimated using ImageJ. MATLAB 2018a was used to generate 154 histograms and determine the average particle sizes. 155 X-ray photoelectron spectroscopy (XPS) was performed in a PHI Quantera SXM Scanning X-ray 156 Microprobe with Al Kα (1486.6 eV) as the excitation source. The binding energy was calibrated by setting the adventitious carbon (corresponding to C-C bonds) to 284.8 eV. High-resolution 157

- spectra were acquired with a pass energy of 23.5 eV, an energy step size of 0.2 eV, and a time step of 50 ms.
- 160 Energy band gap measurements where performed by UV-vis Diffuse Reflectance Spectroscopy
- 161 (UV-vis DRS) and were recorded in a Hitachi UV-vis Spectrophotometer U-2001 using BaSO<sub>4</sub>
- as the reference. The bandgaps were determined based on the Kubelka-Munk function:  $F(R) = (1 + 1)^{-1}$
- $(163 R)^2/2R$ .

168

169

170

171

172

173

174

175

176

177

178

179

- Zeta-potential measurements were performed in a Zetasizer Nano (Malvern) using the zeta
- potential transfer standard DTS 1235. The samples were measured with 500 mg/mL of each
- nanomaterial at pH values varying from 2 to 10, adjusted with either HCl or NaOH.

# Dissolution Measurements of Nanoparticles at different pH values

Dissolution experiments were conducted at different pH values (2, 5, 7 and 10) and at room temperature (≈ 25 °C). A mass of 10 mg of MoO<sub>3</sub> nanoparticles was dispersed in 30 mL of deionized water with adjusted pH using either HCl or NaOH prior to the addition of the nanoparticles. The nanoparticles' dissolution was evaluated for up to seven days (after 30 min, 1 h, 4 h, 6 h, 24 h, 48 h, 96 h, and 168 h in solution). For each time point, a 5 mL sample was taken and filtered with 0.2 μm Nylon filters, and then centrifuged using Amicon ultrafiltration devices (30,000 NMWL) to ensure that all solid particles were removed from the solution. After the filtration, the solutions were measured by flame atomic adsorption spectrometry (AAS) (AAnalyst 200, Perkin Elmer) using a Molybdenum lamp from Perkin Elmer. Five standard solutions with known Mo concentrations were prepared as calibration standards. Exact concentrations of Mo in the sample solutions were obtained using the working calibration curve generated from the standard solution data. The averages and standard deviations of triplicate

measurements were reported for all dissolution measurements. The supernatant of each experiment was collected and characterized by XPS and UV-vis, to determine the nature of the ion.

The isolated ion from the nanorods was also employed at a concentration of 500 mg/L for the evaluation of the interaction between MB and the ion using UV-Vis spectroscopy, degradation of MB using HPLC, and ROS production. Those experiments were performed using the same conditions as the ones for the nanoparticles described below.

# **Photocatalytic Activity Experiments**

180

181

182

183

184

185

186

187

188

189

190

191

192

193

194

195

196

197

198

199

200

201

202

Photocatalytic experiments were carried out at different pH values, varying from 2 to 10 to measure the amount of discoloration of methylene blue (MB) in aqueous suspensions of MoO<sub>3</sub>, which were exposed to visible light (Nexlux LED light, which utilizes the 5050 RGB LED package with a wavelength range of 460 to 630 nm and maximum intensities of 100, 400, and 100 mcd for the red, green, and blue regions, respectively). The initial concentration of MB was fixed at 50 mg/L with a catalyst loading of 500 mg/L and a final volume of 20 mL. Prior to photooxidation, the solution was stirred in the dark for 30 min to establish an adsorptiondesorption equilibrium [2,32]. During irradiation, 1 mL of the mixture solution was withdrawn every 30 min, and then centrifuged (Thermo Scientific Sorvall Legend XTR Centrifuge) at 10,000 rpm for 10 min to separate photocatalysts from the mixture. The extent of MB decomposition was determined by measuring the absorbance values on a UV-Vis spectrometer using a SynergyMX Microtiter plate reader (Biotek) at  $\lambda = 664$  nm. The experiments were performed in triplicates. The results were analyzed and reported as discoloration of MB or MB photocatalytic degradation. The data for the MB discoloration in the light conditions included both adsorption of MB to the nanoparticle and photocatalytic degradation. For the discoloration

in the dark, any MB discoloration reported, corresponded to just adsorption of MB to the nanoparticle. In the case of photocatalytic degradation, the data corresponded to the true photocatalytic activity of the nanoparticles. For the photocatalytic degradation, the discoloration of MB at the end of the light reaction was subtracted from the MB discoloration (adsorption) obtained at the end of the reaction in the dark.

# **Reactive Oxygen species detection**

Reactive oxygen species (ROS) detection was evaluated from pH 2 to 10 by quantifying the production of different species. The concentration of singlet oxygen ( $^{1}O_{2}$ ) was determined by monitoring the concentration of furfuryl alcohol (FFA), as previously described [33]. Hydroxyl radical ( $^{*}OH$ ) was evaluated by the analysis of the degradation of terephthalic acid [33]. The loss of thiol in glutathione (GSH) was used as an indirect method to measure hydrogen peroxide ( $^{*}H_{2}O_{2}$ ) production by nanomaterials. [34]

### Loss of glutathione

MoO<sub>3</sub> nanoparticles and ions, were investigated for hydrogen peroxide production in triplicate by measuring the loss of thiol in GSH. Briefly, 0.4 mM GSH was allowed to react for 2 h at room temperature with samples containing 500 mg/L of MoO<sub>3</sub> or [MoO<sub>4</sub>]<sup>2-</sup> negative controls with non-oxidative agent (H<sub>2</sub>O<sub>2</sub>), and positive controls containing hydrogen peroxide (30%). All the samples where tested in dark and light conditions. After which, 100 mM of Ellman's reagent in Tris-HCl 100 mM was introduced into each tube and allowed to react for 10 min. Then, the nanoparticles were removed by filtration using a 0.2 μm syringe filter (Corning, U.S.A.). The absorbance of the filtrate was read at 412 nm using a Synergy MX Microtiter plate reader to

measure the loss of thiols. The results were expressed as the loss of GSH and represented by Eq. (1) [34].

226 
$$ROS\ production\ (\%) = \frac{Negative\ control\ absorbance - Sample\ absorbance}{Negative\ control\ absorbance} \times\ 100$$

228 Eq. (1)

231 Hydroxyl radical

The production of hydroxyl radical was evaluated via the analysis of the hydroxylation of terephthalic acid (TA) to form fluorescent species. The fluorescent species of 2-hydroxylterephthalic acid was measured at 425 nm in the Synergy MX Microtiter plate reader. Negative controls (without nanoparticles) and positive controls (TA) were also analyzed. A concentration of 500 mg/L of the nanoparticles or [MoO<sub>4</sub>]<sup>2-</sup> were allowed to react with 2 mM of TA. After 2 hours, the nanoparticles were removed by filtration with 0.2 µm nylon filters, and the 2-hydroxylterephthalic acid generated in the samples were quantified by fluorescence using a Synergy MX Microtiter plate reader. The fluorescence intensity was read at an emission wavelength of 425 nm in the fluorescence spectra for 312 nm excitation wavelength [35–37]. The results were expressed using Eq. (1).

242 Singlet oxygen

Singlet oxygen species were evaluated from previously reported methods [38,39]. Briefly, 500 mg/L of each nanoparticle or the isolated ion were mixed with 0.5 mL of furfuryl alcohol (10 µM). Positive and negative controls without nanoparticles were analyzed. When the reaction was

completed, after 2 hours, the nanoparticles were removed by filtration using 0.2  $\mu$ m nylon filters and analyzed by high performance liquid chromatography (HPLC). The chromatographic measurements were carried out on a HPLC Agilent technologies 1290 Infinity with a Zorbax Eclipse Plus C18 4.6 × 150 mm, 5  $\mu$ m column. The mobile phase was H<sub>2</sub>O:MeOH (80:20) %. The flow rate was 1 mL/min, and the injection volume was 20  $\mu$ L. The concentration of  $^{1}$ O<sub>2</sub> was calculated by the integration of the peak area for  $\lambda$  = 219 nm observed at a retention time of 2.6 min in the chromatographs and expressed by Eq (1).

# Product analysis and identification

The MB and its degraded products were separated and identified based on the literature [40]. The MB degradation products were analyzed and separated on the HPLC system described above, with the UV-vis diode array detector set to record the absorbance at 600 nm. The mobile phase was made from acetonitrile (solution A) and buffer solution (solution B). The buffer solution was 0.1M ammonium acetate and acetic acid (pH 5.3). The gradient elution was a linear gradient from 5% A to 95% A in 30 min, at a total flow rate of 0.8 mL/min, and the injection volume was 100μL.

### Scavenger experiments

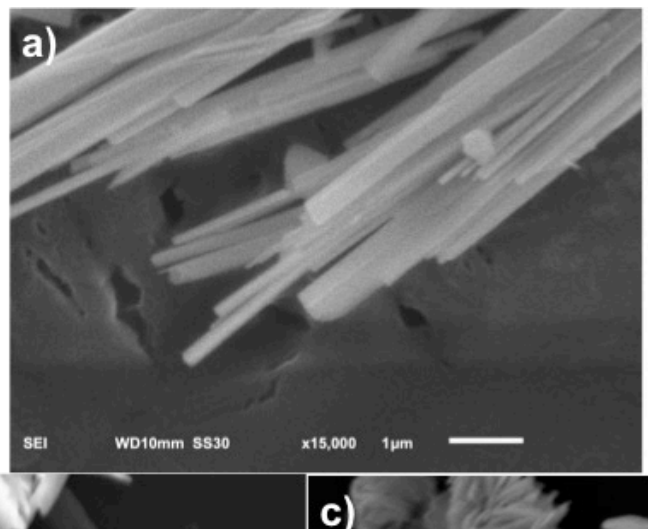
Isopropyl alcohol (IPA), triethanolamine (TEOA) and p-benzoquinone (p-BQ), were added to the reaction in order to evaluate the degradation mechanisms. The experiments were performed for the nanorods at pH 5.4 employing the same procedure as the one described in the photocatalytic activity experiments. Briefly, 50 mg/mL of MB with 500 mg/L of the nanomaterial in a final volume of 20 mL was prepared. To each reaction, 10 mM of TEOA, 75 mM of IPA and 1 mM of p-BQ were employed. After 30 min stirring in the dark to

establish an adsorption-desorption equilibrium, the samples were irradiated. An aliquot of 1 ml of sample was collected every 30 min and then centrifuged. The absorbance at  $\lambda = 664$  nm was measured to analyze the discoloration of MB.

# **Results and Discussion**

# 3.1. Synthesis and characterization of the nanoparticles

Three MoO<sub>3</sub> nanoparticles with different morphologies were successfully synthesized, as shown in Figure 1. All the nanoparticles showed smooth surfaces, as well as regular and monodisperse shapes and structures. The nanowires and nanorods presented diameters in the range of 59 nm and 180 nm, respectively. The nanosheets had a thickness around 74 nm and a width of approximately 180 nm. Both the nanorods and nanowires presented lengths greater than 5  $\mu$ m.



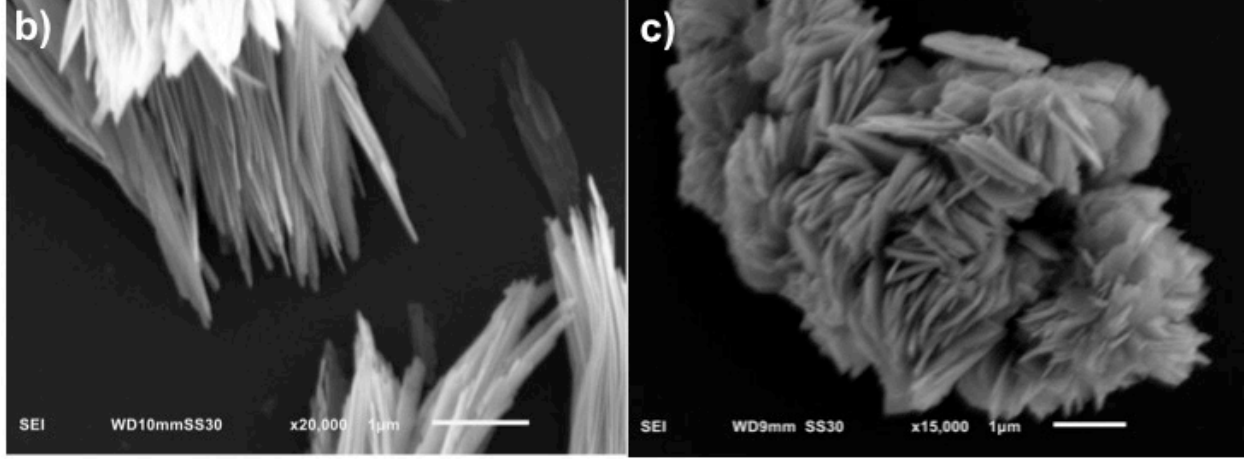


Figure 1: SEM images of a) nanorods b) nanowires and c) nanosheets. The scale bars correspond to 1 µm size.

The chemical and crystalline structures of the nanoparticles were determined by XRD, FT-IR spectroscopy, and XPS. The normalized FT-IR spectrum of the MoO<sub>3</sub> nanoparticles is shown in the Supporting Information (Figure S1). The bands around 972, 969, and 984 cm<sup>-1</sup> are associated with the Mo=O stretching vibration. The bands around 896, 708, and 840 cm<sup>-1</sup> are associated with the Mo-O-Mo stretching, and the bands at 517, 555 and 538 cm<sup>-1</sup> are the result of the O-Mo<sub>3</sub> single bonds [41–43]. The weak peaks located around 1400 and 1600 cm<sup>-1</sup> are related to the presence of the crystallization of water in the crystals of the MoO<sub>3</sub> nanoparticles. The nanorods show peaks in the 800-1000 cm<sup>-1</sup> and 500 to 600 cm<sup>-1</sup> ranges indicating presence of the Mo=O

bond and Mo-O bonds, respectively. Similarly, the nanosheets present both bond types as the nanorods. However, the nanowires seem to have an increased presence of single bonds as observed with the 538 nm peak. The nanosheets do not have such a strong presence of the Mo-O single bonds. The Mo=O to Mo-O ratios shown in Table 1 confirm this analysis since the nanowires double bond to single bond ratio is nearly half of that of the nanorods and nanosheets.

XRD patterns for the MoO<sub>3</sub> nanoparticles are shown in Figure S2. The strong diffraction peaks demonstrate that the samples are highly crystalline. For the nanosheets and nanowires most of the peaks for these samples are indexed as orthorhombic MoO<sub>3</sub> (JCPDS – 35-0569) and for the nanorods as hexagonal (JCPDS – 21-0569). Using the Scherrer equation [44,45] and the FWHMs, the crystal sizes of the nanowires, nanosheets, and nanorods were calculated to be 32 nm, 29 nm, and 33 nm, respectively. The difference in sizes with those of the extrapolated sizes from the SEM images could be due to peak broadening caused by crystal lattice strain or lattice defects [46–48].

The surface chemistry of the nanoparticles as well as the chemical states of the MoO<sub>3</sub> nanoparticles were analyzed by XPS as shown in Figure 2. The Mo 3d spectra for all the nanoparticles present different oxidative states. The spectrum for the nanorods shows presence of the EB (Mo <sup>3</sup>d<sub>5/2</sub>) <sup>1</sup>/<sub>4</sub> 233.15 eV and EB (Mo <sup>3</sup>d<sub>3/2</sub>) <sup>1</sup>/<sub>4</sub> 236.3 eV corresponding to Mo<sup>6+</sup>; however the spectra of nanowires and nanosheets exhibit the presence of the bands (Mo <sup>3</sup>d<sub>5/2</sub>) <sup>1</sup>/<sub>4</sub> 231.78 eV and EB (Mo <sup>3</sup>d<sub>3/2</sub>) <sup>1</sup>/<sub>4</sub> 234.92 eV, which indicate the existence of Mo<sup>5+</sup>. In Table 1, the calculation of the ratio of peak/area is shown. As we can see, the different morphologies showed different fractional amounts of Mo<sup>6+</sup> and Mo<sup>5+</sup>, indicating that the nanoparticle with a higher amount of Mo<sup>5+</sup> contains large quantities of oxygen vacancies, which have been introduced during the synthesis of the nanomaterial. The presence of these vacancies causes a deficiency of

O<sub>2</sub> in the crystal structure, which causes a decrease in the energy band gap [49] as evident in Table 1. This decrease in the energy band gap is desirable as previous studies have shown that it can increase the photocatalytic properties of the material by allowing greater absorption of light.[50] The bandgaps of all three material are less than 3 eV making the material capable of absorbing visible and UV light. While from the XRD patterns the nanowires and nanosheets appear to have similar crystal structures, in the XPS the nanowires and nanorods appear chemically more similar. This could be a result of the growth mechanism during synthesis resulting in different vacancies in each nanoparticle. Based on these results, the composition of the nanorods and nanowires nanoparticles is similar regarding the oxidation states, however their structure is different due to the different growth mechanisms during synthesis. The differences in the chemical and physical structure of these nanomaterials could affect their stability, which is discussed later based on the dissolution stability of the different MoO<sub>3</sub> nanoparticles.

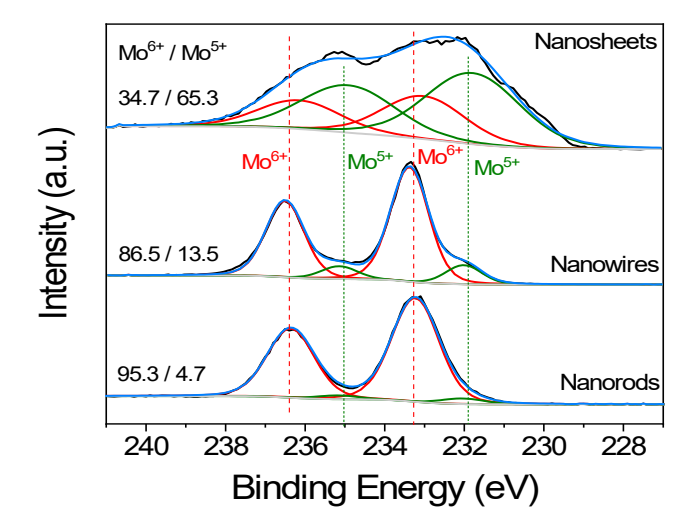


Figure 2: XPS of all MoO<sub>3</sub> nanoparticles.

| Nanapartiala | Mean Size (nm) |      | I <sub>Mo-</sub> n) O/I <sub>Mo=O</sub> | Mo <sup>6+</sup> | Mo <sup>5+</sup> | Mo <sup>6+</sup> : Mo <sup>5+</sup> | Energy bandgap |
|--------------|----------------|------|---|------------------|------------------|-------------------------------------|----------------|
| Nanoparticle | From           | From |   | NIO              | WIO              | ratio                               | (eV)           |
|              | SEM            | XRD  |   |                  |                  |                                     |                |
| Nanorods     | 180            | 32   | 0.77                                    | 95.3             | 4.7              | 20.3                                | 2.93           |
| Nanowires    | 59             | 29   | 0.48                                    | 86.5             | 13.5             | 6.41                                | 2.95           |
| Nanosheets   | 74             | 33   | 0.99                                    | 34.7             | 65.3             | 0.531                               | 2.64           |

# 3.2. Stability of MoO<sub>3</sub> nanoparticles in aqueous solutions

Previous studies have described that the dissolution rate of nanoparticles can be affected by the size, crystallinity, shape, surface area, and exposed plane, among other factors [20]. The dissolution of the MoO<sub>3</sub> nanoparticles was analyzed from pH 2 to 10 for a period of 1 week, as shown in Figure 3. Interestingly, for all the nanoparticles, the dissolution was only partial, i.e., the nanoparticles did not dissolve completely (*i.e.*, up to 100 mg/L of MoO<sub>3</sub> was dissolved) and eventually reached a plateau. The nanowires dissolved the most (e.g., around 80% (260 mg/L of MoO<sub>3</sub>) after 1 week at pH 10), compared to the nanosheets, which presented the lowest dissolution (< 20% at all pH conditions). These results seem to be directly correlated to the presence of the Mo-O single bonds and double bonds, as well as the different oxidative states. For instance, the nanowires presented the highest dissolution as well as the strongest presence of Mo-O single bonds as seen in the FTIR results compared to the nanosheets (Figure S1). In the case of the oxidative state, the nanosheets presented Mo<sup>5+</sup> state as opposed to the nanowires and nanorods that had Mo<sup>6+</sup> oxidative states and also higher dissolutions (Table 1).

Further analysis of the Mo ionic species dissolved through XPS and UV-vis spectroscopy (Figure S3) showed that for all the nanoparticles, the primarily dissolved ion was Mo<sup>6+</sup>. These results are in accordance with the literature that the majority of the dissolution of the nanoparticles are with Mo<sup>6+</sup> oxidative state (e.g. nanowires and nanorods) [51–54]. Aqueous solutions of Mo<sup>6+</sup> ions have been studied in detail showing a dependency on the ion concentration and pH. Previous studies have shown that at low Mo concentrations, the predominant species in aqueous solutions is the monomeric tetrahedral [MoO4]<sup>2-</sup> ion [55,56]. In summary, the dissolution of the MoO3 nanoparticles depends on the pH of the media. The

In summary, the dissolution of the MoO<sub>3</sub> nanoparticles depends on the pH of the media. The higher the pH, the greater the dissolution. The extent by which the particles dissolve in solution, however, seems to be dependent on the oxidation state and type of oxygen bonds found in the nanoparticles [15].

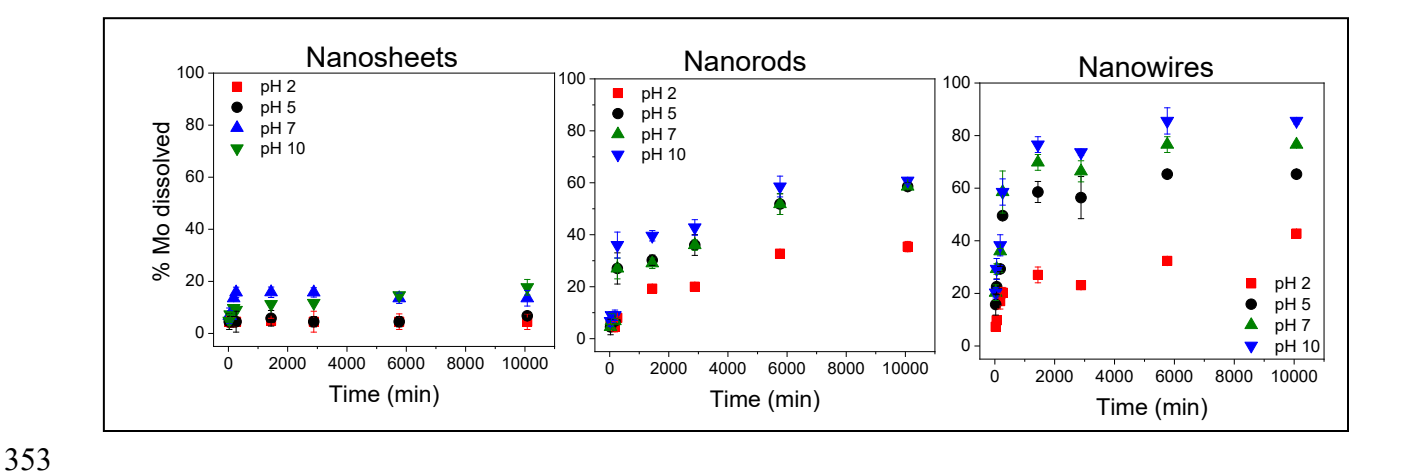


Figure 3: Representation of %Mo dissolved vs. time at different pH values. From left to right, in order of increasing dissolution, nanosheets, nanorods, and nanowires.

# 3.3. MB interactions with MoO<sub>3</sub> nanoparticles

Initial investigation of the interaction of MB with the nanoparticles was determined via ATR-FTIR (Figure S4). The results showed that the nanoparticle surface adsorbs MB. The differences between the ATR-FTIR spectra of the MoO<sub>3</sub> with MB in the dark and light showed the combination of bands of MoO<sub>3</sub> and MB and also a small shift to higher cm<sup>-1</sup> for some of the bands (for instance, the MB band at 880 shifts to 897 in the dark and to 884 in the light, and the MB band at 1596 cm<sup>-1</sup> shifts slightly to 1601 cm<sup>-1</sup> and 1602 cm<sup>-1</sup> for MB adsorbed to the nanoparticles in the light and dark, respectively). To estimate the electric charge on the nanoparticle surface and elucidate the ability of MB to adsorb onto the nanoparticles, zeta potential measurements were performed. The magnitude of the zeta potential provides information about particle stability. Figure S5 represents the zeta potential for all the nanoparticles vs. pH. When the pH of the media increased, the zeta potential values for the nanorods and nanosheets decreased while the zeta potential for the nanosheets increased slightly before decreasing slightly again. These patterns follow the degradation pattern due to light, as illustrated in Figure 5, indicating that due to the increasingly negative surface charge at higher pH values the degradation decreases. This could be caused by the increased adsorbance of the MB (a positively charged molecule) to the nanoparticles at higher pH values, which will decrease the ability of the nanoparticles to absorb light.

358

359

360

361

362

363

364

365

366

367

368

369

370

371

372

373

374

375

376

377

378

379

380

To verify whether degradation of MB or mere adsorption or complexation was taking place XPS was utilized. The XPS results on the surface of the nanoparticles (Figure S6) showed a decrease in the pyridinic acid band when compared to the MB XPS indicating that photocatalytic degradation of MB is taking place. Furthermore, the decrease in the pyridinic band was greater for the samples that were irradiated than for those kept in the dark.

The fact that all the nanoparticles exhibited similar behavior with regards to their ability to

decolorize MB, the evaluation of the degradation byproducts of MB was performed for the nanorod MoO<sub>3</sub>. Figure 4 shows the chromatographic separation of the methylene blue in dark and light conditions after 2 hours of reaction at pH 5.4. The data showed that MB was significantly degraded under light irradiation, while some adsorption was observed when the reaction was placed in the dark. The decrease in the methylene blue peak intensity and the appearance of new peaks at lower retention times have been reported previously [57]. Consequently, photocatalysis of dye solutions not only caused its discoloration, but also an appreciable degree of transformation of the dye molecule.

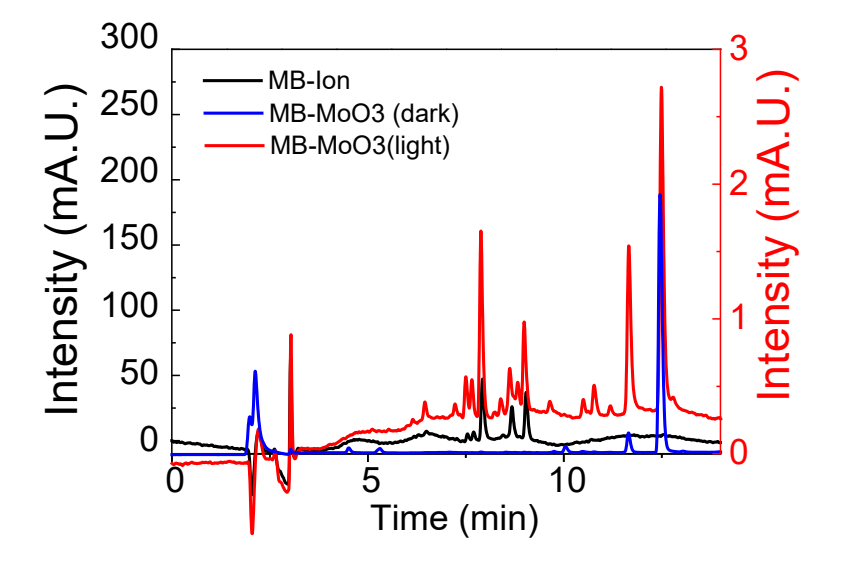


Figure 4: HPLC analysis of the reaction between the nanorods and methylene blue after 2 hours in light and dark conditions. MB-ion and MB-MoO3 (light) left axes and MB-MoO3 (dark) right axes.

In the case of the ions, the HPLC results of the reaction between the ions and methylene blue also showed some degradation byproducts. From the results, when the reaction is performed in

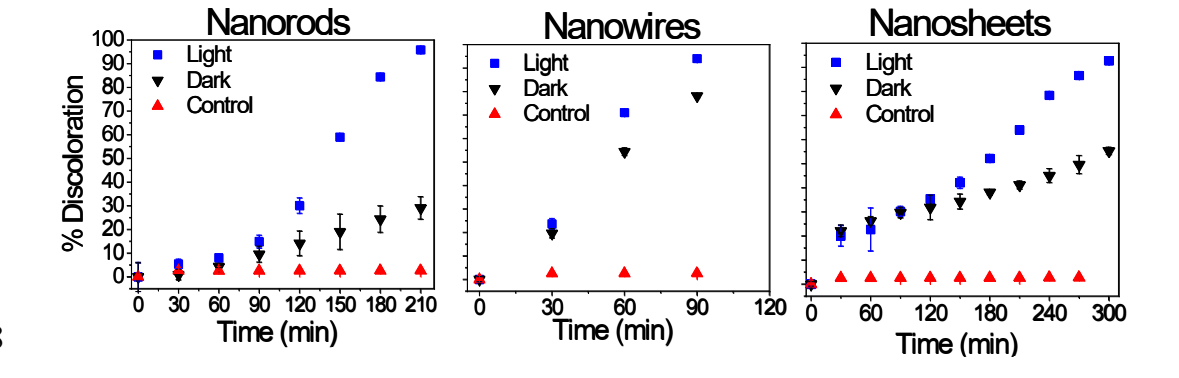
the dark (Figure 4 blue curve), the chromatograms do not show any peaks at lower retention times as opposed to light. The strong interaction between methylene blue and the isolated ions is confirmed with the ATR-FTIR spectra. In the spectra, it is possible to observe a decrease in the OH band for the ion-MB spectra, and the appearance of the MoO<sub>3</sub> band at 550 cm<sup>-1</sup> (Figure S7). This result showed that a MB-Mo ion complexation is happening during the reaction. Figure S8 showed a blue precipitate when the ion is in contact with MB. The small contribution of the ions in the degradation process and the complexation observed by ATR-FTIR showed that both processes are happening simultaneously. That means that the peaks in the chromatogram are degradation byproducts and not complexes. These results confirm that the ions are also participating in the degradation process.

# 3.4. Photocatalytic activity of the nanoparticles and ions with MB

In this investigation, we tried to understand the role of the nanoparticles' characteristics in relation to their ability to decolorize MB (Figure 5) and true photocatalytic activity (Figure 6). In the decolorization assay (Figure 5), both adsorption and photocatalytic phenomena were reported for the light exposure; while in the dark only adsorption is observed. In the case of the photocatalytic percentage discoloration (Figure 6), it was reported the photocatalytic activity after subtraction of the discoloration reaction of MB in the dark and light conditions to show the amount each material was able to decolorize solely due to the influence of the light exposure, i.e. photocatalysis (Figure 6). All three materials were able to decolorize MB as shown in Figure 5, however, the nanorods displayed greater photocatalytic percentage discoloration, therefore was considered to have the best photocatalytic activity. While, the nanowires displayed the least photocatalytic activity.

In the case of the rate of discoloration of MB, herein defined as the time it took for the each nanomaterial to decolorize MB, shown in Figure 5 as the final timepoint of each discoloration experiment, the nanowires had the fastest reaction rate, which was capable of decolorizing MB after 90 minutes; while the nanorods decolorized MB after 210 minutes and the nanosheets after 300 minutes. The rate at which each nanoparticle decolorized MB could be explained in terms of the stability of the nanoparticle. The nanowires, which were the particles that showed the highest dissolution, were the ones showing the highest reaction rate.

These results indicate that the photocatalytic activity of the material is not directly or completely related to the band gap energy of the material or the relative percentages of the different oxidation states of the Mo (Table 1). The nanorods presented the highest photocatalytic activity, while they had the second largest band gap and the largest ratio of Mo<sup>+6</sup> to Mo<sup>+5</sup> ions. The nanosheets presented the lowest photocatalytic activity, even though they had the smallest bandgap and smallest ratio of Mo<sup>+6</sup> to Mo<sup>+5</sup> ions. This indicates that while a smaller band gap can be beneficial in allowing greater absorption of light, it can also increase electron-hole pair recombination rates, thereby reducing the ability of the material to produce ROS. Hence, based on these results, the oxidation state seems to be playing an exceedingly significant role in the material's photocatalytic properties.



In order to confirm the role of dissolution on the photocatalytic activity, the photocatalytic degradation results of MB by the nanoparticles were compared against the nanoparticle dissolution at the end of each reaction at different pH values as shown in Figure 6 to understand the role of dissolution on degradation of MB. Increasing the pH from 2 to 10 resulted in enhanced dissolution of the nanorods and nanowires by 40% and 60%, respectively, which was accompanied by a decrease in decolorization of the MB. However, the difference in dissolution of the nanosheets did not show a detrimental impact on the degradation of MB, likely because of the lower extent of dissolution of the nanosheets (< 20% at all pH values over the experimental period).

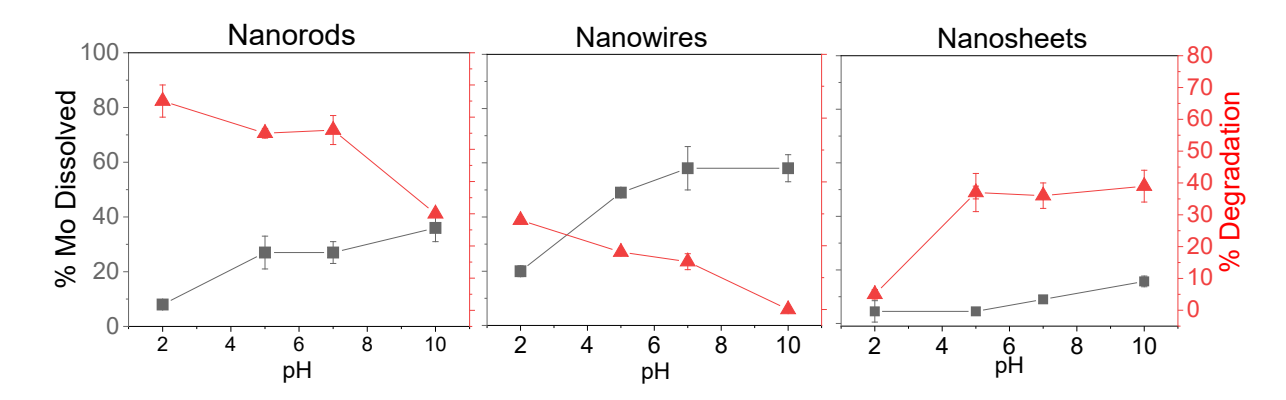
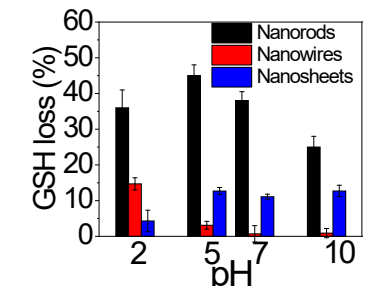


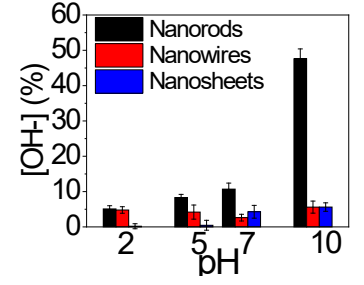
Figure 6: Nanomaterial dissolution and MB degradation after light reaction after subtracting from dark reaction) at different pH values at the end of each experiment. Black dots indicate the % of Mo dissolved and red dots the % of MB degraded.

### 

The photocatalytic degradation mechanism by nanoparticles has been associated with the production of reactive oxygen species. In this study, the production of different ROS was evaluated for all three nanomaterials to better understand the degradation mechanisms of MoO<sub>3</sub> nanoparticles under visible light represent the production of OH<sup>-</sup>, <sup>1</sup>O<sub>2</sub> and H<sub>2</sub>O<sub>2</sub> radicals at different pH values, since pH clearly showed an important role in the photocatalytic activity of the MoO<sub>3</sub> nanoparticles. Among the three different MoO<sub>3</sub> structures investigated, the nanorods produced the most ROS, which explains the increased photocatalytic activity of this nanomaterial as seen in Figure 5. In fact, the presence of light directly affected the ROS production of the nanorods, as seen in Figures S9-S11.

More importantly, all three nanomaterials showed production of ROS even in dark conditions indicating that the nanomaterial not only have photocatalytic properties, but also catalytic properties. Furthermore, the production of ROS increased with increasing pH values. Figure 7 shows the contribution of ROS production due to the introduction of visible light for the different nanoparticles at the different pH values. As we can see, the increase in pH increases the concentration of hydroxyl ions in solution, which can promote the formation of H<sub>2</sub>O<sub>2</sub>, following oxidation reactions leading to the formation of singlet oxygen or undergoing reduction by forming hydroxyl radicals. The low amount formation of  $^{1}$ O<sub>2</sub> can be explained because the singlet oxygen radical is not produced via electron transfer process [58].





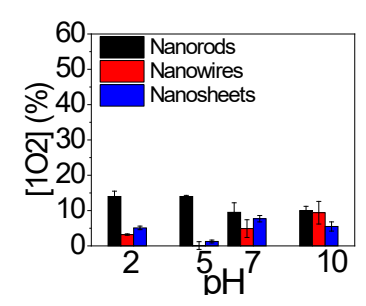


Figure 7: ROS production difference between light and dark for each nanomaterial at each pH value.

Interestingly, if we compare the degradation results in Figure 6 with the production of the ROS in Figure 7, specifically the hydrogen peroxide production of the nanorods, nanowires, and nanosheets, we see similar patterns indicating that the most probable primary species responsible for the degradation of MB is hydrogen peroxide. For instance, with increasing pH, the hydrogen peroxide production contribution from the light of the nanorods and nanowires generally decreases as does the % degradation in Figure 6. However, the hydrogen peroxide production of the nanosheets increases slightly and then remains approximately the same as pH 2 exhibiting the same pattern as the % degradation in Figure 6.

The ROS from the isolated ions produced by the nanoparticles were also evaluated in the present study. In Figure S12, it is evident that the ion resulting from the dissolution of the nanomaterial can have degradative effects due to ROS production. In the dark condition, hydroxyl radical and hydrogen peroxide production are not significant; while in the presence of light, there is a significant increase in these ROS. This finding signifies that the dissolved ions from the nanomaterial can also contribute to the degradation of MB.

In order to further understand the role of ROS in the photocatalytic mechanism of the MoO<sub>3</sub> nanoparticles, we employed ROS scavengers and a hole scavenger. Isopropyl alcohol (IPA) was employed to trap  $\cdot$ OH, triethanolamine (TEOA) scavenges h+ and benzoquinone (BQ) scavenges  $\cdot$ O<sub>2</sub><sup>-</sup> [59–62]. These scavengers were added to the reaction and the degradation results are shown in Figure 8.

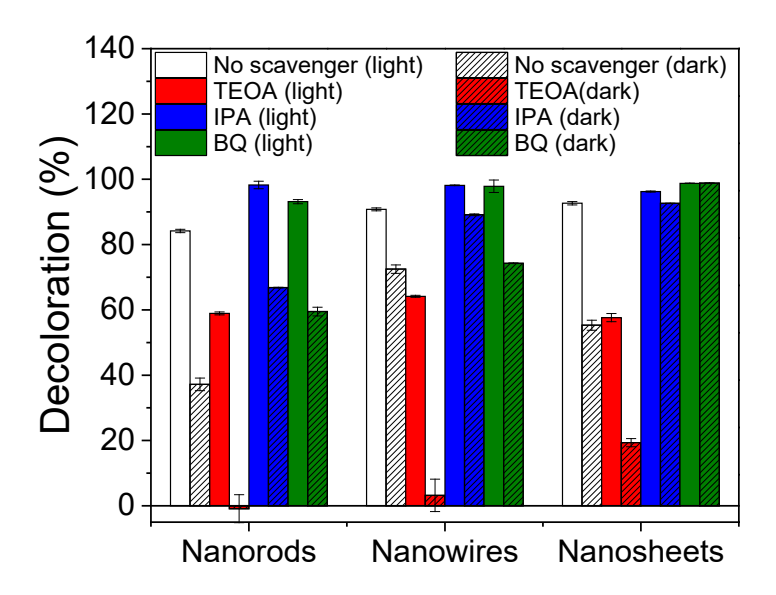


Figure 8: MB degradation with each of the nanomaterial in the presence of scavengers in light and dark conditions. Reaction conditions were 500 mg/mL of MoO3 at pH 5.4 in the presence of 10 mM of TEOA, 75 mM of IPA and 1 mM of p-BQ.

In the presence of reactants that act as ROS scavengers, the degradative properties of the nanoparticles were reduced. The greatest effect was seen with the addition of TEOA, which is a hole scavenger, as shown in Figure 8. Only with the presence of TEOA all three nanomaterials were unable to completely decolorize MB, indicating that the production of holes plays an important role in MB degradation. However, when the reaction takes place in the dark in the presence of TEOA, no discoloration is observed. In this case, TEOA seems to act as a competing adsorbent able to inhibit the MB adsorption on the surface of the nanoparticles. Furthermore, this confirms that the likely pathway by which hydrogen peroxide is generated is via the oxidation of water molecules by the photogenerated holes. In addition, hydrogen peroxide is the

most likely primary species responsible for the degradation of methylene blue since, when hydroxyl and singlet oxygen scavengers were added, complete degradation of MB was still possible. Interestingly, when isopropanol was present (a hydroxyl radical scavenger) the photocatalytic reaction became more efficient. A possible explanation could be that the generation of additional water molecules from the isopropanol and hydroxyl radical reaction may get oxidized by the photogenerated holes further increasing hydrogen peroxide concentrations.

# **Conclusions**

In the present work, we have successfully synthesized MoO<sub>3</sub> nanoparticles with different sizes, morphologies, and properties. We have demonstrated that the dissolution process depends on the oxidative state, and nature of the Mo-O bond- For instance, the nanosheets, which contained more Mo<sup>5+</sup> than Mo<sup>6+</sup>, dissolved less than the nanorods which had more Mo<sup>6+</sup> rather than Mo<sup>5+</sup> in their structure.

The photocatalytic experiments of methylene blue showed that the photocatalytic degradation of MB is influenced by the dissolution of the nanomaterials. Furthermore, there is a relationship between the degradation and complexation process. The dissolved ions can play an important role in the photocatalytic activity of the nanoparticle. As shown in the HPLC experiments, the ion not only produces a complex between the MB, but it is also able to degrade MB.

While ROS production and subsequent degradation of MB were observed by the nanomaterial, some ROS production was observed by the dissolved product of the nanomaterial. We also quantified the production of different ROS and we saw that hydrogen peroxide is the most important ROS responsible for the degradation of MB. The analysis of the ROS and the employment of different scavengers showed that H<sub>2</sub>O<sub>2</sub> and the photogenerated holes in the

nanoparticles play a role in the degradation process of methylene blue. The photogenerated holes increased the oxidation of water molecules while increasing the concentration of H<sub>2</sub>O<sub>2</sub>, the ROS responsible for the degradation of MB.

Funding

This work was supported by the NSF BEINM Grant Number: 1705511, and the Welch foundation award number (E-2011-20190330) The findings achieved herein are solely the

responsibility of the authors.

- 545 [1] M. Santos-Beltran, F. Paraguay-Delgado, R. Garcia, W. Antunez-Flores, C. Ornelas-546 Gutierrez, A. Santos-Beltran, Fast methylene blue removal by MoO3 nanoparticles, J. 547 Mater. Sci. Mater. Electron. 28 (2017) 2935–2948. doi:10.1007/s10854-016-5878-2.
- 548 [2] A. Chithambararaj, N.S. Sanjini, A.C. Bose, S. Velmathi, Flower-like hierarchical h-549 MoO3: new findings of efficient visible light driven nano photocatalyst for methylene 550 blue degradation, Catal. Sci. Technol. (2013). doi:10.1039/c3cy20764a.
- 551 [3] A. Manivel, G.J. Lee, C.Y. Chen, J.H. Chen, S.H. Ma, T.L. Horng, J.J. Wu, Synthesis of MoO3 nanoparticles for azo dye degradation by catalytic ozonation, Mater. Res. Bull. (2015). doi:10.1016/j.materresbull.2014.11.016.
- 554 [4] N. Pernicone, F. Lazzerin, G. Liberti, G. Lanzavecchia, The oxidation of methanol over pure MoO3 catalyst, J. Catal. 14 (1969) 391–393. doi:http://dx.doi.org/10.1016/0021-9517(69)90331-5.
- 557 [5] C.I. Fernandes, S.C. Capelli, P.D. Vaz, C.D. Nunes, Highly selective and recyclable 558 MoO3 nanoparticles in epoxidation catalysis, Appl. Catal. A Gen. 504 (2015) 344–350. 559 doi:10.1016/j.apcata.2015.02.027.
- F. Dwivedi, S. Dhanekar, S. Das, Synthesis of α -MoO 3 nano- fl akes by dry oxidation of RF sputtered Mo thin fi lms and their application in gas sensing, Semicond. Sci. Technol. 31 (n.d.) 1–7. doi:10.1088/0268-1242/31/11/115010.
- R.B. Pujari, V.C. Lokhande, V.S. Kumbhar, N.R. Chodankar, C.D. Lokhande, Hexagonal microrods architectured MoO3 thin film for supercapacitor application, J. Mater. Sci. Mater. Electron. 27 (2016) 3312–3317. doi:10.1007/s10854-015-4160-3.
- 566 [8] D.-T. Nguyen, S. Vedraine, L. Cattin, P. Torchio, M. Morsli, F. Flory, J.C. Bernède, 567 Effect of the thickness of the MoO 3 layers on optical properties of MoO 3 /Ag/MoO 3 568 multilayer structures, J. Appl. Phys. 112 (2012) 063505. doi:10.1063/1.4751334.
- J.S. Chen, Y.L. Cheah, S. Madhavi, X.W. Lou, Fast synthesis of α-MoO3 nanorods with controlled aspect ratios and their enhanced lithium storage capabilities, J. Phys. Chem. C. 114 (2010) 8675–8678. doi:10.1021/jp1017482.
- 572 [10] X.W. Lou, H.C. Zeng, Hydrothermal synthesis of α-MoO3 nanorods via acidification of ammonium heptamolybdate tetrahydrate, Chem. Mater. 14 (2002) 4781–4789. doi:10.1021/cm0206237.
- 575 [11] A. Phuruangrat, D.J. Ham, S. Thongtem, J.S. Lee, Electrochemical hydrogen evolution 576 over MoO3 nanowires produced by microwave-assisted hydrothermal reaction, 577 Electrochem. Commun. 11 (2009) 1740–1743. doi:10.1016/J.ELECOM.2009.07.005.
- 578 [12] V. Kumar, X. Wang, P.S. Lee, Formation of hexagonal-molybdenum trioxide (h-MoO 3 )
  579 nanostructures and their pseudocapacitive behavior †, 7 (2015) 11777.
  580 doi:10.1039/c5nr01505g.

- 581 [13] E.P. Gray, C.L. Browning, M. Wang, K.D. Gion, E.Y. Chao, K.J. Koski, A.B. Kane, R.H. Hurt, Biodissolution and cellular response to MoO3 nanoribbons and a new framework for early hazard screening for 2D materials, Environ. Sci. Nano. 5 (2018) 2545–2559. doi:10.1039/c8en00362a.
- 585 [14] Z. Wang, W. Zhu, Y. Qiu, X. Yi, A. Von Dem Bussche, A. Kane, H. Gao, K. Koski, R. Hurt, Biological and environmental interactions of emerging two-dimensional nanomaterials, Chem. Soc. Rev. 45 (2016) 1750–1780. doi:10.1039/c5cs00914f.
- 588 [15] S. Kittler, C. Greulich, J. Diendorf, M. Köller, M. Epple, Toxicity of silver nanoparticles 589 increases during storage because of slow dissolution under release of silver ions, Chem. 590 Mater. 22 (2010) 4548–4554. doi:10.1021/cm100023p.
- 591 [16] K. Loza, J. Diendorf, C. Sengstock, L. Ruiz-Gonzalez, J.M. Gonzalez-Calbet, M. Vallet-592 Regi, M. Köller, M. Epple, The dissolution and biological effects of silver nanoparticles in 593 biological media, J. Mater. Chem. B. 2 (2014) 1634–1643. doi:10.1039/c3tb21569e.
- 594 [17] W. Vogelsberger, Thermodynamic and Kinetic Considerations of the Formation and the 595 Dissolution of Nanoparticles of Substances Having Low Solubility, J. Phys. Chem. B. 107 596 (2003) 9669–9676. doi:10.1021/jp030347z.
- 597 [18] E.A. Meulenkamp, Size Dependence of the Dissolution of ZnO Nanoparticles, J. Phys. 598 Chem. B. 102 (1998) 7764–7769. doi:10.1021/jp982305u.
- T. Xia, M. Kovochich, M. Liong, M. Schowalter, A. Rosenauer, B. Gilbert, J.I. Zink, a.
   E. Nel, L. Mädler, Comparison of the Mechanism of Toxicity of Zinc Oxide and Cerium
   Oxide Nanoparticles Based on Dissolution and Oxidative Stress Properties, Chemie Ing.
   Tech. 81 (2009) 1167–1167. doi:10.1002/cite.200950629.
- 603 [20] S.K. Misra, A. Dybowska, D. Berhanu, S.N. Luoma, E. Valsami-Jones, The complexity of nanoparticle dissolution and its importance in nanotoxicological studies, Sci. Total Environ. 438 (2012) 225–232. doi:10.1016/j.scitotenv.2012.08.066.
- E.P. Gray, C.L. Browning, M. Wang, K.D. Gion, E.Y. Chao, K.J. Koski, A.B. Kane, R.H. Hurt, Biodissolution and cellular response to MoO3 nanoribbons and a new framework for early hazard screening for 2D materials, Environ. Sci. Nano. 5 (2018) 2545–2559. doi:10.1039/c8en00362a.
- 610 [22] D. Wang, L. Zhao, L.H. Guo, H. Zhang, Online Detection of reactive oxygen species in ultraviolet (UV)-irradiated nano-TiO2 suspensions by continuous flow chemiluminescence, Anal. Chem. 86 (2014) 10535–10539. doi:10.1021/ac503213m.
- 613 [23] Y. Nosaka, A.Y. Nosaka, Generation and Detection of Reactive Oxygen Species in Photocatalysis, Chem. Rev. 117 (2017) 11302–11336. doi:10.1021/acs.chemrev.7b00161.
- Y. Guo, C. Cheng, J. Wang, Z. Wang, X. Jin, K. Li, P. Kang, J. Gao, Detection of reactive oxygen species (ROS) generated by TiO2(R), TiO2(R/A) and TiO2(A) under ultrasonic and solar light irradiation and application in degradation of organic dyes, J. Hazard. Mater. 192 (2011) 786–793. doi:10.1016/j.jhazmat.2011.05.084.
- Y. Li, W. Zhang, J. Niu, Y. Chen, Mechanism of photogenerated reactive oxygen species and correlation with the antibacterial properties of engineered metal-oxide nanoparticles,

- 621 ACS Nano. 6 (2012) 5164–5173. doi:10.1021/nn300934k.
- 622 [26] A.S. Adeleye, X. Wang, F. Wang, R. Hao, W. Song, Y. Li, Photoreactivity of graphene 623 oxide in aqueous system: Reactive oxygen species formation and bisphenol A 624 degradation, Chemosphere. 195 (2018) 344–350. doi:10.1016/j.chemosphere.2017.12.095.
- 625 [27] O. Choi, Z. Hu, Size dependent and reactive oxygen species related nanosilver toxicity to nitrifying bacteria, Environ. Sci. Technol. 42 (2008) 4583–4588. doi:10.1021/es703238h.
- 627 [28] M.J. Akhtar, M. Ahamed, S. Kumar, M.A. Majeed Khan, J. Ahmad, S.A. Alrokayan, Zinc 628 oxide nanoparticles selectively induce apoptosis in human cancer cells through reactive 629 oxygen species, Int. J. Nanomedicine. 7 (2012) 845–857. doi:10.2147/IJN.S29129.
- 630 [29] K. Buyukhatipoglu, A.M. Clyne, Superparamagnetic iron oxide nanoparticles change 631 endothelial cell morphology and mechanics via reactive oxygen species formation, J. 632 Biomed. Mater. Res. - Part A. 96 A (2011) 186–195. doi:10.1002/jbm.a.32972.
- 633 [30] A. Chithambararaj, A.C. Bose, Hydrothermal synthesis of hexagonal and orthorhombic 634 MoO3 nanoparticles, J. Alloys Compd. 509 (2011) 8105–8110. 635 doi:10.1016/j.jallcom.2011.05.067.
- 636 [31] H. Yin, Y. Kuwahara, K. Mori, H. Cheng, M. Wen, Y. Huo, H. Yamashita, Localized Surface Plasmon Resonances in Plasmonic Molybdenum Tungsten Oxide Hybrid for Visible-Light-Enhanced Catalytic Reaction, J. Phys. Chem. C. 121 (2017) 23531–23540. doi:10.1021/acs.jpcc.7b08403.
- 640 [32] Y. Chen, C. Lu, L. Xu, Y. Ma, W. Hou, J.J. Zhu, Single-crystalline orthorhombic 641 molybdenum oxide nanobelts: Synthesis and photocatalytic properties, CrystEngComm. 642 12 (2010) 3740–3747. doi:10.1039/c000744g.
- 643 [33] A.S. Adeleye, X. Wang, F. Wang, R. Hao, W. Song, Y. Li, Photoreactivity of graphene 644 oxide in aqueous system: Reactive oxygen species formation and bisphenol A 645 degradation, Chemosphere. 195 (2018) 344–350. doi:10.1016/j.chemosphere.2017.12.095.
- J. Peña-Bahamonde, V. San Miguel, H.N. Nguyen, R. Ozisik, D.F. Rodrigues, J.C.
   Cabanelas, Functionalization of reduced graphene oxide with polysulfone brushes enhance
   antibacterial properties and reduce human cytotoxicity, Carbon N. Y. 111 (2017) 258–
   268. doi:10.1016/j.carbon.2016.10.005.
- 650 [35] A.S. Adeleye, X. Wang, F. Wang, R. Hao, W. Song, Y. Li, Photoreactivity of graphene 651 oxide in aqueous system: Reactive oxygen species formation and bisphenol A 652 degradation, Chemosphere. 195 (2018) 344–350. 653 doi:10.1016/J.CHEMOSPHERE.2017.12.095.
- 654 [36] D. Jassby, J. Farner Budarz, M. Wiesner, Impact of Aggregate Size and Structure on the 655 Photocatalytic Properties of TiO <sub>2</sub> and ZnO Nanoparticles, Environ. Sci. Technol. 46 656 (2012) 6934–6941. doi:10.1021/es202009h.
- 657 [37] X. Xu, D. Chen, Z. Yi, M. Jiang, L. Wang, Z. Zhou, X. Fan, Y. Wang, D. Hui, 658 Antimicrobial mechanism based on H 2 O 2 generation at oxygen vacancies in ZnO 659 crystals, Langmuir. 29 (2013) 5573–5580. doi:10.1021/la400378t.

- 660 [38] A.A. Dayem, M.K. Hossain, S. Bin Lee, K. Kim, S.K. Saha, G.M. Yang, H.Y. Choi, S.G. Cho, The role of reactive oxygen species (ROS) in the biological activities of metallic nanoparticles, Int. J. Mol. Sci. 18 (2017) 1–21. doi:10.3390/ijms18010120.
- 663 [39] W.R. Haag, J. Hoigne', E. Gassman, A. Braun, Singlet oxygen in surface waters Part I: 664 Furfuryl alcohol as a trapping agent, Chemosphere. 13 (1984) 631–640. 665 doi:10.1016/0045-6535(84)90199-1.
- 666 [40] M.A. Rauf, M. Meetani, A. Khaleel, Photocatalytic Degradation of Methylene Blue Using 667 a Mixed Catalyst and Product Analysis by LC / MS, (2010). 668 doi:10.1016/j.cej.2009.11.017.
- 669 [41] G.A. Nazri, C. Julien, Far-infrared and Raman studies of orthorhombic MoO3 single crystal, Solid State Ionics. 53–56 (1992) 376–382. doi:10.1016/0167-2738(92)90403-C.
- 671 [42] T. Hirata, In-situ observation of Mo-O stretching vibrations during the reduction of MoO3 with hydrogen by diffuse reflectance FTIR spectroscopy, Appl. Surf. Sci. 40 (1989) 179–181. doi:10.1016/0169-4332(89)90174-8.
- 674 [43] W.P. Griffith, Oxy-complexes and their vibrational spectra, J. Chem. Soc. A Inorganic, Phys. Theor. (1969) 211. doi:10.1039/j19690000211.
- [44] S.B. Rathod, M.K. Lande, B.R. Arbad, A.B. Gambhire, Preparation, characterization and catalytic activity of MoO3/CeO2-ZrO2 solid heterogeneous catalyst for the synthesis of β-enaminones, Arab. J. Chem. 7 (2014) 253–260. doi:10.1016/j.arabjc.2010.10.027.
- 679 [45] D. Sundeep, A. Gopala Krishna, R.V.S.S.N. Ravikumar, T. Vijaya Kumar, S. Daniel 680 Ephraim, Y.L. Pavan, Spectral characterization of mechanically synthesized MoO3-CuO 681 nanocomposite, Int. Nano Lett. 6 (2016) 119–128. doi:10.1007/s40089-015-0178-z.
- 682 [46] A. Monshi, M.R. Foroughi, M.R. Monshi, Modified Scherrer Equation to Estimate More 683 Accurately Nano-Crystallite Size Using XRD, World J. Nano Sci. Eng. 02 (2012) 154– 684 160. doi:10.4236/wjnse.2012.23020.
- 685 [47] G. Fagherazzi, M. Battagliarin, A. Benedetti, S. Enzo, A profile-fitting procedure for analysis of broadened X-ray diffraction peaks. II. Application and discussion of the methodology, 1988. http://journals.iucr.org/j/issues/1988/05/00/ms0241/ms0241.pdf (accessed April 5, 2019).
- 689 S. Ott, P.G. Sanders, A. Borbe, J.R. Weertman, T. Unga, Dislocations, Grain Size and 690 Planar Faults in Nanostructured Copper Determined By High Resolution X-Ray 691 Diffraction and New Procedure of Peak Profile Analysis, 1998. 692 https://pdf.sciencedirectassets.com/271635/1-s2.0-S1359645400X00304/1-s2.0-
- 693 S1359645498000019/main.pdf?x-amz-security-
- token=AgoJb3JpZ2luX2VjED4aCXVzLWVhc3QtMSJGMEQCIFAAo01VsR2vZiSCc6a
   B%2Bv%2FS9TDTnB2pBzzPU4nZfMRTAiAClCPd905dcfZFiH8dRj7XhgTJswH4IgZm
   VB8nHoTi (accessed April 5, 2019).
- [49] K. Inzani, M. Nematollahi, F. Vullum-Bruer, T. Grande, T.W. Reenaas, S.M. Selbach,
   Electronic properties of reduced molybdenum oxides, Phys. Chem. Chem. Phys. 19 (2017)
   9232–9245. doi:10.1039/c7cp00644f.

- 700 [50] S. Zhu, D. Wang, Photocatalysis: Basic principles, diverse forms of implementations and emerging scientific opportunities, Adv. Energy Mater. 7 (2017). doi:10.1002/aenm.201700841.
- 703 [51] T. Ozeki, H. Kihara, S. Ikeda, Study of equilibria in 0.03 mM molybdate acidic aqueous solutions by factor analysis applied to ultraviolet spectra, Anal. Chem. 60 (1988) 2055–2059. doi:10.1021/ac00170a014.
- 706 [52] W. Swartz, D.M. Hercules, X-ray photoelectron spectroscopy of molybdenum 707 compounds. Use of electron spectroscopy for chemical analysis (ESCA) in quantitative 708 analysis, Anal. Chem. 43 (1971) 1774–1779. doi:10.1021/ac60307a020.
- 709 [53] G. Davis, W.C. Moshier, G.D. Davis, Interaction of Molybdate Anions with the Passive Film on Aluminum Interaction of Molybdate Anions with the Passive Film on Aluminum\*, (2015). doi:10.5006/1.3585065.
- 712 [54] J.-G. Choi, L.T. Thompson, XPS study of as-prepared and reduced molybdenum oxides, Appl. Surf. Sci. 93 (1996) 143–149. doi:10.1016/0169-4332(95)00317-7.
- [55] J. Aveston, E.W. Anacker, J.S. Johnson, Hydrolysis of Molybdenum(VI).
   Ultracentrifugation, Acidity Measurements, and Raman Spectra of Polymolybdates, Inorg.
   Chem. 3 (1964) 735–746. doi:10.1021/ic50015a030.
- 717 [56] R.H. Busey, O.L. Keller, Structure of the Aqueous Pertechnetate Ion by Raman and Infrared Spectroscopy. Raman and Infrared Spectra of Crystalline KTcO 4, KReO 4, Na 2 MoO 4, Na 2 WO 4, Na 2 MoO 4 · 2H 2 O, and Na 2 WO 4 · 2H 2 O, J. Chem. Phys. 41 (1964) 215–225. doi:10.1063/1.1725625.
- 721 M.A. Rauf, M. Meetani, A. Khaleel, M.A. Rauf, M.A. Meetani, A. Khaleel, A. Ahmed, 722 Photocatalytic Degradation of Methylene Blue Using a Mixed Catalyst and Product Eng. 723 Analysis by LC/MS, Artic. Chem. J. 373-378. 157 (2010)724 doi:10.1016/j.cej.2009.11.017.
- 725 [58] H. Xu, W.J. Cooper, J. Jung, W. Song, Photosensitized degradation of amoxicillin in natural organic matter isolate solutions, Water Res. 45 (2011) 632–638. doi:10.1016/J.WATRES.2010.08.024.
- 728 [59] M. Zhong, Z. Wei, X. Meng, F. Wu, J. Li, From MoS2 microspheres to α-MoO3 nanoplates: Growth mechanism and photocatalytic activities, Eur. J. Inorg. Chem. 2014 (2015) 3245–3251. doi:10.1002/ejic.201402079.
- [60] Z. Liu, Y. Jin, F. Teng, X. Hua, M. Chen, An efficient Ce-doped MoO 3 catalyst and its photo-thermal catalytic synergetic degradation performance for dye pollutant, CATCOM. 66 (2015) 42–45. doi:10.1016/j.catcom.2015.03.017.
- 734 [61] A. Chithambararaj, N.S. Sanjini, A. Chandra Bose, S. Velmathi, Flower-like hierarchical h-MoO 3: new findings of efficient visible light driven nano photocatalyst for methylene blue degradation †, Catal. Sci. Technol. 3 (2013) 1405. doi:10.1039/c3cy20764a.
- 737 [62] Y. Liu, P. Feng, Z. Wang, X. Jiao, F. Akhtar, Novel fabrication and enhanced 738 photocatalytic MB degradation of hierarchical porous monoliths of MoO3 Nanoplates, 739 Sci. Rep. 7 (2017). doi:10.1038/s41598-017-02025-3.